

# THE STELLAR POPULATION AND STAR FORMATION RATES OF $Z \approx 1.5$ – $1.6$ [O II] EMITTING GALAXIES SELECTED FROM NARROW-BAND EMISSION-LINE SURVEYS

CHUN LY,<sup>1,9</sup> MATTHEW A. MALKAN,<sup>2</sup> NOBUNARI KASHIKAWA,<sup>3,4</sup> MASAO HAYASHI,<sup>3</sup> TOHRU NAGAO,<sup>5,6</sup> KAZUHIRO SHIMASAKU,<sup>7,8</sup> KAZUAKI OTA,<sup>6</sup> AND NATHANIEL R. ROSS<sup>2</sup>

Received 2012 May 31

## ABSTRACT

We present the first detailed study of the stellar populations of star-forming galaxies at  $z \sim 1.5$ , which are selected by their [O II] emission line, detected in narrow-band surveys. We identified  $\sim 1,300$  [O II] emitters at  $z = 1.47$  and  $z = 1.62$  in the Subaru Deep Field with rest-frame EWs above  $13\text{\AA}$ . Optical and near-infrared spectroscopic observations for  $\approx 10\%$  of our samples show that our separation of [O II] from [O III] emission-line galaxies in two-color space is 99% successful. We analyze the multi-wavelength properties of a subset of  $\sim 1,200$  galaxies with the best photometry. They have average rest-frame EW of  $45\text{\AA}$ , stellar mass of  $3 \times 10^9 M_{\odot}$ , and stellar age of 100 Myr. In addition, our SED fitting and broad-band colors indicate that [O II] emitters span the full range of galaxy populations at  $z \sim 1.5$ . We also find that 80% of [O II] emitters are also photometrically classified as “BX/BM” (UV) galaxies and/or the star-forming “BzK” (near-IR) galaxies. Our [O II] emission line survey produces a far more complete, and somewhat deeper sample of  $z \sim 1.5$  galaxies than either the BX/BM or sBzK selection alone. We constructed average SEDs and find that higher [O II] EW galaxies have somewhat bluer continua. SED model-fitting shows that they have on average half the stellar mass of galaxies with lower [O II] EW. The observed [O II] luminosity is well-correlated with the far-UV continuum with a logarithmic slope of  $0.89 \pm 0.22$ . The scatter of the [O II] luminosity against the far-UV continuum suggests that [O II] can be used as a SFR indicator with a reliability of 0.23 dex.

*Subject headings:* galaxies: photometry — galaxies: distances and redshifts — galaxies: evolution — galaxies: high-redshift — infrared: galaxies — ultraviolet: galaxies

## 1. INTRODUCTION

Since the star formation rate (SFR) density of galaxies is an order of magnitude higher at  $z \approx 1$ – $5$  than in the local universe (e.g., Hopkins 2004), emission-line galaxies are prominent in the young universe, and thus are useful probes of the evolution of galaxies. Current techniques to identify such emission-line galaxies include grism surveys (Shim et al. 2009; Atek et al. 2010; Coil et al. 2011; Straughn et al. 2011), slit spectroscopy (e.g., DEEP2; Davis et al. 2003), and narrow-band imaging (e.g., Malkan et al. 1996; Teplitz et al. 1998; Fujita et al. 2003; Hippelein et al. 2003; Ly et al. 2007, hereafter L07). Narrow-band surveys have identified large samples of star-forming galaxies by detecting their redshifted nebular emission lines, at low and intermediate redshifts, to as high as  $z \sim 7$ . These surveys have the ability to: (1) determine redshift to 1 percent accuracy, (2) derive emission-line fluxes, which can be used to determine star-formation rates (SFRs) and trace the evo-

lution of the cosmic SFR density. And they accomplish this with roughly an order-of-magnitude higher efficiency than spectroscopic surveys.

However, it is still unclear what galaxy population(s) these techniques probe or are unable to probe. For example, it might be that these surveys are biased towards the youngest and possibly least reddened galaxies. Such claims have been made for Ly $\alpha$  emitters when compared to Lyman break galaxies at similar redshifts (e.g., Gawiser et al. 2007). Thus, it is crucial to understand the selection bias of current and future emission-line surveys using these techniques. Our survey utilizes  $\sim 1,300$  [O II] emitters at  $z = 1.47$  and  $z = 1.62$  in the Subaru Deep Field (SDF; Kashikawa et al. 2004).

The outline of this paper is as follows. In Section 2, we discuss the SDF and the optical imaging that we have acquired and reduced. Section 3 discusses the selection of narrow-band (NB) excess emitters, the spectroscopic observations, the technique to separate [O II] emitters from H $\alpha$  and [O III], and the photometric redshifts. Section 4 presents the results on the [O II] EW distributions, a comparison between the rest-frame UV luminosity and the [O II] luminosity, their stellar population from modeling the spectral energy distribution (SED), and compares the [O II] population against popular color selection techniques at these redshifts. We then summarize our conclusions in Section 5. Throughout this paper, we adopt a flat cosmology with  $\Omega_{\Lambda} = 0.7$ ,  $\Omega_M = 0.3$ , and  $H_0 = 70 \text{ km s}^{-1} \text{ Mpc}^{-1}$ , and magnitudes are reported on the AB system (Oke 1974).

## 2. THE SUBARU DEEP FIELD OBSERVATIONS

chunly@stsci.edu

<sup>1</sup> Space Telescope Science Institute, Baltimore, MD, USA

<sup>2</sup> Department of Physics and Astronomy, UCLA, Los Angeles, CA, USA

<sup>3</sup> Optical and Infrared Astronomy Division, National Astronomical Observatory, Mitaka, Tokyo, Japan

<sup>4</sup> Department of Astronomy, School of Science, Graduate University for Advanced Studies, Mitaka, Tokyo, Japan

<sup>5</sup> The Hakubi Project, Kyoto University, Kyoto, Japan

<sup>6</sup> Department of Astronomy, Kyoto University, Kyoto, Japan

<sup>7</sup> Department of Astronomy, School of Science, University of Tokyo, Bunkyo, Tokyo, Japan

<sup>8</sup> Research Center for the Early Universe, School of Science, University of Tokyo, Tokyo, Japan

<sup>9</sup> Giacomini Fellow.

Several extragalactic fields already have deep imaging in NB filters with Subaru/Suprime-Cam (Miyazaki et al. 2002). Of all of these, the SDF has the most sensitive optical NB imaging in six NB filters in the sky, and is further complemented with deep multi-band imaging between  $1500\text{\AA}$  and  $4.5\mu\text{m}$ . The most prominent emission lines entering these NB filters are  $\text{H}\alpha$ ,  $[\text{O III}] \lambda 5007$ , and  $[\text{O II}] \lambda\lambda 3726, 3729$ , at well-defined redshift windows between  $z \approx 0.07$  and  $z \approx 1.62$ .

### 2.1. NB921 and NB973 Imaging Observations

For this paper, we focus on excess emitters found using two filters, NB921 and NB973. Their central wavelengths and FWHM are  $9196\text{\AA}$  and  $132\text{\AA}$  for NB921 and  $9755\text{\AA}$  and  $200\text{\AA}$  for NB973. The acquisition of the SDF NB921 data has already been discussed in Kashikawa et al. (2004), Kashikawa et al. (2006), and L07. The NB921 data are identical to the publicly released SDF v.1 data.<sup>10</sup> The NB973 data were acquired on 2005 March 16–17 and 2007 May 9 for a total integration time of 21.5 h (Iye et al. 2006; Ota et al. 2008). The seeing varied between  $0''.5$  and  $1''.0$  and observing conditions were photometric in 2005 but not in 2007.

Both the NB921 and NB973 data were reduced using SDFRED (Yagi et al. 2002; Ouchi et al. 2004), a software package designed solely for Suprime-Cam data. The spatial resolutions for the final NB921 and NB973 mosaics are  $0''.96$  and  $0''.91$ , respectively.

By repeatedly measuring the flux within  $2''$  diameter apertures at random positions in the mosaics, we determined that the  $3\sigma$  limits for the NB921 and NB973 data are 26.60 and 25.64 mag, respectively. A summary of the sensitivity in other wave-bands, that are later discussed, can be found in Table 1 of Ly et al. (2011). The publicly available  $z'$ -band mosaicked image, which is used throughout this paper, has a  $3\sigma$  sensitivity of 26.83 mag, while the  $i'$ -band data (later used) is 0.93 mag deeper.

### 3. SELECTION OF NARROW-BAND EXCESS EMITTERS

The NB921- and NB973-detected catalogs were obtained by running SExtractor (Bertin & Arnouts 1996, vers. 2.5.0). The unmasked regions cover  $870.4 \text{ arcmin}^2$  for NB921 and  $788.7 \text{ arcmin}^2$  for NB973. The latter is smaller due to higher systematic noise in one of the ten CCDs, which was masked to avoid significant spurious detections. A total of 119,541 and 84,786 sources were detected in the unmasked regions of the NB921 and NB973 images, respectively.

To select NB excess emitters, the standard technique is to compare the flux in the NB against the flux in an adjacent broad-band filter. We use the  $z'$ -band, since it samples the local continuum around these NB filters. Fluxes from the  $z'$ -band were extracted by running SExtractor in “dual-image” mode, where the respective NB image was used as the “detection” image. This works well because all three mosaicked images have very similar seeing, so the  $z'$ -NB colors are determined within the same physical scale of the galaxies. For the extraction of fluxes and selection of sources, we use a  $2''$  diameter circular aperture, which encloses 17 kpc at  $z \approx 1.5$ .

<sup>10</sup> <http://soaps.nao.ac.jp/SDF/v1/index.html>.

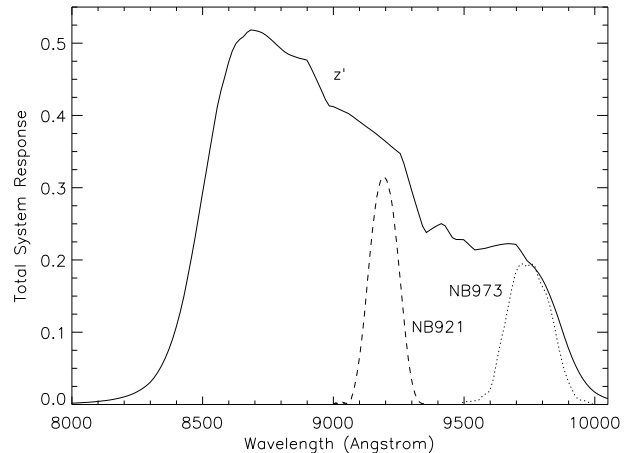


FIG. 1.— Total system throughput for the  $z'$  (solid), NB921 (dashed), and NB973 (dotted) filters.

One minor issue affecting the NB921 and NB973 filters is that they are located redward of the  $z'$ -band sensitivity peak,  $\sim 8700\text{\AA}$  (see Figure 1). For redder galaxies, this makes the  $z'$ -NB colors systematically higher, and could falsely identify lineless red galaxies as NB-excess emitters.

To resolve this issue, we empirically estimate the continuum flux at the wavelengths of the NB filters by fitting the  $i'$ - $z'$  and  $z'$ -NB colors for non-NB excess sources:

$$\langle z' - \text{NB921} \rangle_C = -0.003 + 0.077(i' - z'), \text{ and} \quad (1)$$

$$\langle z' - \text{NB973} \rangle_C = -0.014 + 0.271(i' - z'). \quad (2)$$

These relations are consistent with simple linear extrapolations of the  $i'$ - $z'$  color to  $9200\text{\AA}$  or  $9755\text{\AA}$ . The corrected  $z'$ -NB color is then

$$\Delta(z' - \text{NB}) = (z' - \text{NB}) - \langle z' - \text{NB} \rangle_C. \quad (3)$$

To illustrate the reliability of these corrections, we plot the  $z'$ -NB973 colors with and without the color-term correction for NB973 emitters in Figure 2. This correction was not performed previously for the NB921 excess emitter sample identified by L07. It has a minor effect for the NB921 sample, but is more important for the NB973 sample since the NB973 filter is significantly redder by an additional  $\sim 560\text{\AA}$ . For example, we find that the rms in the  $z'$ -NB color (at the bright end) is decreased by 10% for NB921 and 50% for NB973 when this correction is applied (see Figure 2). Since the minimum threshold for selection (discussed below) is driven by the observed scatter, such a reduction permits us to select toward lower minimum  $z'$ -NB excesses.

In Figure 3, we illustrate the corrected  $z'$ -NB921 and  $z'$ -NB973 colors for NB921- and NB973-detected sources, respectively. For selecting objects with genuine NB921 and NB973 excesses, we require minimum  $z'$ -NB magnitude differences of 0.20 mag (observed EW of  $32\text{\AA}$ ) and 0.25 mag (observed EW of  $70\text{\AA}$ ), respectively. These minima are 5.6 and 6.7 times the rms of the  $z'$ -NB color at the luminous end. The observed EW is determined from a combination of the broad- and narrow-band fluxes, and is given by:

$$\text{EW}_{\text{obs}} = \Delta\text{NB} \left[ \frac{f_{\lambda, \text{NB}} - f_{\lambda, z}}{f_{\lambda, z} - f_{\lambda, \text{NB}}(\Delta\text{NB}/\Delta z)} \right], \quad (4)$$

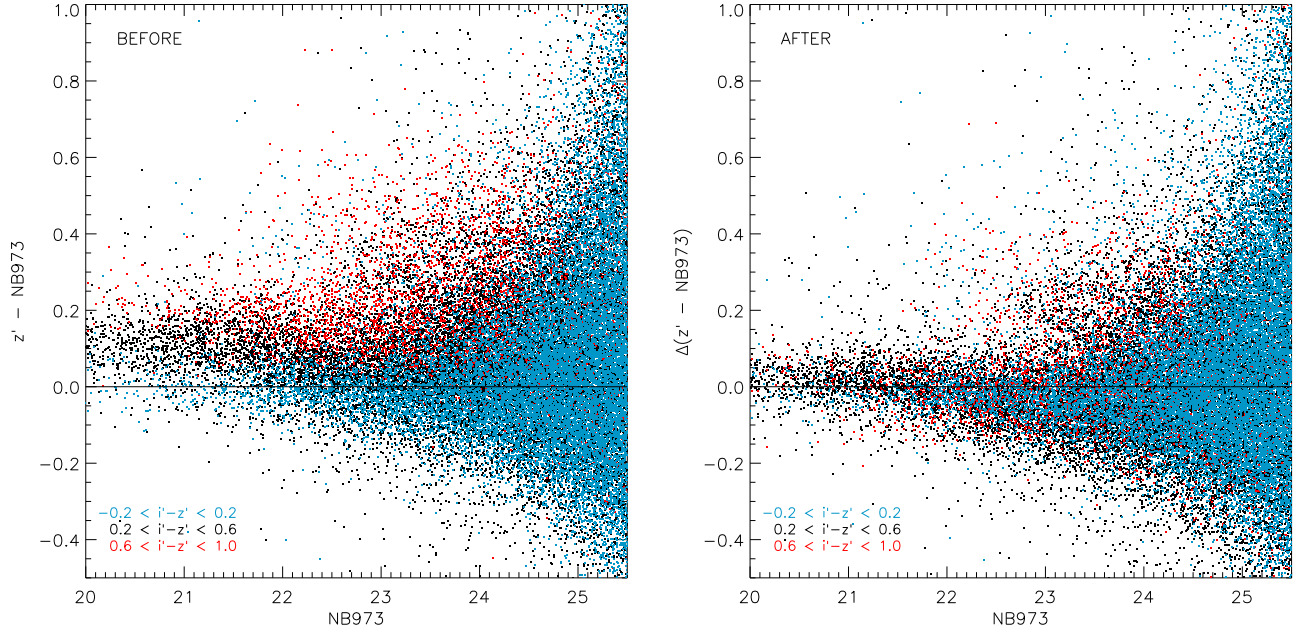


FIG. 2.—  $z'$ -NB973 colors for NB973 excess emitters as measured (left) and after applying the  $i'-z'$  color-term correction given in Equation (2) (right). Cyan, black, and red squares denote galaxies with blue, intermediate, and red  $i'-z'$  colors. The color-term correction ensures that red galaxies with weak or absent [O II] emission are not falsely classified as NB973 excess emitters.

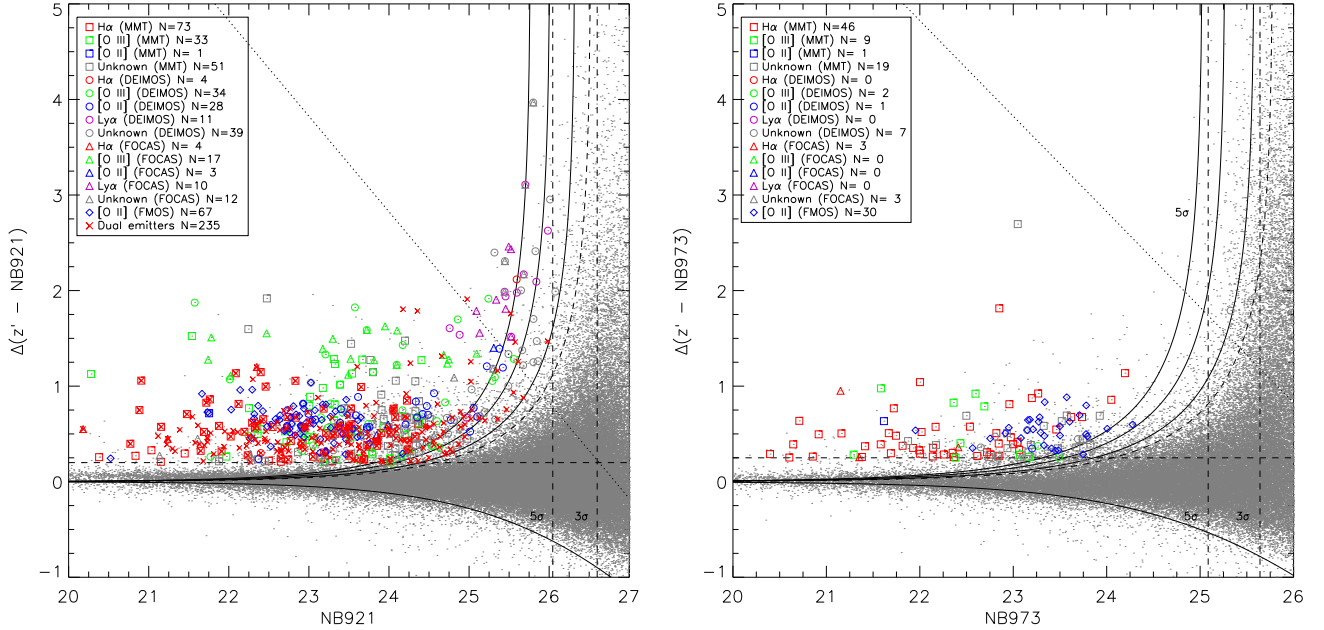


FIG. 3.—  $\Delta(z'-\text{NB})$  for NB921 (left) and NB973 (right) samples (grey points) in the SDF. The  $3\sigma$  and  $5\sigma$  sensitivity limits for the NB data are shown as vertical dashed lines. Minimum excesses of 0.2 mag (left) and 0.25 mag (right) are illustrated with the horizontal dashed lines. Also overlaid are curves for  $N \times \sigma_{z'-\text{NB}}$  with  $N = 2.5$  (dashed line) and 3.0, 4.0, and 5.0 (solid lines). Sources that fall above the diagonal dotted lines are undetected in the  $z'$ -band at  $3\sigma$ . In the absence of noise, the strongest possible magnitude excess is  $\approx 2.5$  magnitudes, which corresponds to a pure emission line centered in the NB filter, and no continuum. Spectroscopically confirmed sources are overlaid with symbols representing different instruments: DEIMOS (circles), Hectospec (squares), FOCAS (triangles), and FMOS (diamonds). Red crosses represent galaxies that are dual excess emitters in both the NB704 and NB921 bands (see Section 3.1.2). H $\alpha$ , [O III], [O II], and Ly $\alpha$  are distinguished by red, green, blue, and purple colors, respectively. Also overlaid in grey symbols are the cases where an emission line was not detected in the spectra.



where  $\Delta\text{NB}$  and  $\Delta z$  (955Å) are the FWHMs for the narrow-band and  $z'$ , respectively, and  $f_{\lambda,X}$  is the flux density in  $\text{erg s}^{-1} \text{cm}^{-2} \text{Å}^{-1}$  in band “X” (L07). We also require that the  $z'$ -NB color exceeds

$$3\sigma_{z'-\text{NB}}(\text{NB}) \equiv -2.5 \log \left( 1 - \frac{\sqrt{f_{\nu,3\sigma\text{NB}}^2 + f_{\nu,3\sigma z'}^2}}{f_{\nu,\text{NB}}} \right), \quad (5)$$

where  $f_{\nu,3\sigma X}$  is the  $3\sigma$  flux density limit for band “X” and  $f_{\nu,\text{NB}}$  is the flux density for a given NB magnitude. These selection criteria yield 2512 NB921 excess emitters and 1666 NB973 excess emitters. The  $3\sigma$  emission-line flux limits are  $5.8 \times 10^{-18}$  and  $1.7 \times 10^{-17} \text{ erg s}^{-1} \text{cm}^{-2}$  for NB921 and NB973, respectively. Smaller samples were also constructed by requiring stronger detections of  $4\sigma_{z'-\text{NB}}$  and  $5\sigma_{z'-\text{NB}}$ . These samples contain 1912 and 1616 for NB921 and 839 and 565 for NB973.

While the color-term corrections (see Equations (1)–(2)) should apply to galaxies with SEDs that behave simply, at  $z \sim 1.3$ – $1.4$  the 4000Å break falls in the  $z'$ -band, but is blueward of the NB filter. This poses a problem, as galaxies with older stellar populations ( $\gtrsim 1$  Gyr) will have a strong break, and the continuum flux at  $\sim 9200$ Å or 9700Å can easily be underestimated from a linear extrapolation of the  $i'$ - $z'$  color. This population was confirmed when the photometric redshifts (hereafter  $z_{\text{phot}}$ ; see Section 3.3 for further discussion) were derived. At these  $z_{\text{phot}}$ 's, the [O II] emission line does not fall into the NB973 passband. Since these galaxies are very red, simply imposing a cut of  $i'-z' \leq 0.8$  (0.4) for NB921 (NB973), most of these 4000Å-break galaxies can be removed without affecting the true line emitters. By removing these red false NB excess emitters, the NB921 sample is reduced to 2361 ( $3\sigma$ ), 1787 ( $4\sigma$ ), and 1505 ( $5\sigma$ ). Likewise, the NB973 sample is reduced by about 25%–30%, to 1243 ( $3\sigma$ ), 571 ( $4\sigma$ ), and 375 ( $5\sigma$ ).

### 3.1. Independent Confirmation of NB Excesses

#### 3.1.1. Follow-up Spectroscopy of NB Excess Candidates

To confirm that the NB technique efficiently identifies emission-line galaxies, we have conducted spectroscopy with several instruments (both optical and near-infrared) over the past several years. The observations were obtained with Keck’s Deep Imaging Multi-Object Spectrograph (DEIMOS; Faber et al. 2003) in 2004, 2008, and 2009, Subaru’s Faint Object Camera and Spectrograph (FOCAS; Kashikawa et al. 2002) in 2004 and 2007, MMT’s Hectospec (Fabricant et al. 2005) in 2008, and Subaru’s Fiber Multi-object Spectrograph (FMOS; Kimura et al. 2010) in 2012.

The DEIMOS and FOCAS follow-up spectroscopy has been discussed in Kashikawa et al. (2006) and L07, and DEIMOS data that were acquired more recently are discussed in Kashikawa et al. (2011). The Hectospec and FOCAS observations typically had 1–2 hrs of on-source integration, while the DEIMOS observations had 2–4 hrs. In addition, we observed for 2.5–3.0 hrs with FMOS.

For the Hectospec observations, we utilized the 270  $\text{mm}^{-1}$  grating blazed at 5200Å to yield a spectral coverage of 3650Å–9200Å with a spectral resolution of  $\approx 5$ Å. A total of four different fiber configurations were used. The

on-source integration varied between 80 and 140 minutes. The MMT spectra were reduced following standard procedures with the HSRED<sup>11</sup> reduction pipeline.

FMOS observations, which only targeted galaxies suspected to be [O II] emitters (see Section 3.2), were obtained on 2012 8–9 Apr utilizing “cross-beam switching” mode. Each exposure was 15 m in length and obtained with “ABAB” dithering. The data were reduced using FIBRE, a reduction package that consists of IRAF scripts and CFITSIO routines, designed solely for optimal FMOS data reduction (Iwamuro et al. 2011).

A summary of the spectroscopic observations obtained for NB921 and NB973 emitters is provided in Table 1. In total, 522 NB921 emitters and 204 NB973 emitters were targeted. Our NB973 spectroscopic observations are sparser, since that sample became available much later. The majority (70% and 90% for the NB921 and NB973 samples, respectively) of our spectra are from Hectospec and FMOS, with most of the [O II] confirmations from FMOS. Among these spectroscopically targeted NB921 excess emitters,  $\approx 57\%$  (295) have reliable redshifts (based at least one other emission line). Similarly, 51% (104) of the observed NB973 excess emitters yielded clear spectroscopic identifications and redshifts. These success rates were closer to 70% using only the optical spectroscopy, which is generally more sensitive. In addition, we exclude 31 (6%) NB921 and 8 (3%) NB973 sources that show single weak emission lines in their optical spectra which, if they are real, are consistent with the redshifts predicted by an emission line in the NB filter.

The numbers of spectroscopically confirmed H $\alpha$ , [O III]/H $\beta$ , [O II], and Ly $\alpha$  lines are summarized in Table 1. We note that a small subset (9 NB921 and 10 NB973) of our spectroscopic confirmations do not correspond to a strong emission line entering our NB filter. These could be explain by (1) photometric errors, or (2) an old stellar population, which would decrease the  $z'$ -band flux relative to flux at the NB wavelength (see Section 3).

We illustrate in Figure 3, the  $\Delta(z'-\text{NB})$  colors for spectroscopically confirmed sources. The NB921 spectroscopic sample spans six magnitudes in luminosity and three magnitudes in NB921 excess. Because of sparser sampling, the NB973 spectroscopic sample covers four magnitudes in luminosity and one magnitude in NB973 excess. They show that NB921 (NB973) excesses of 0.2 mag (0.25 mag) are indeed due to the presence of weak-but real-emission lines.

#### 3.1.2. Dual Line Detection with NB Filter Pairs

In addition to spectroscopy, another independent approach showing that the NB selection technique efficiently identifies line-emitting galaxies, is a second NB filter that targets another emission line at the identical redshift. Coincidentally, the NB704 filter (centered at 7046Å with a FWHM of 100Å) is able to accomplish this in conjunction with NB921. Others (e.g., Hippelein et al. 2003; Nagao et al. 2008; Nakajima et al. 2012) have exploited similar dual-line instances to confirm emission-line galaxies at a particular redshift. When H $\alpha$  (H $\beta$ ) is redshifted into the NB921 filter at  $z = 0.40$  ( $z = 0.89$ ), [O III] ([O II]) enters the NB704 bandpass. We illustrate in Figure 4 the redshift range probed by these

<sup>11</sup> <http://www.astro.princeton.edu/~rcool/hsred/>.

TABLE 1  
SUMMARY OF SPECTROSCOPIC SAMPLES

Filter (1)	Targeted <sup>1</sup> (2)	Confirmed <sup>1</sup> (3)	Ambiguous <sup>1</sup> (4)	DEIMOS (5)	MMT (6)	FOCAS (7)	FMOS <sup>2</sup> (8)	$N(\text{H}\alpha)$ (9)	$N([\text{O III}])$ (10)	$N([\text{O II}])$ (11)	$N(\text{Ly}\alpha)$ (12)
NB921	522	295	227	88 (127)	113 (164)	36 (48)	68 (212)	81	80	104	21
NB973	204	104	100	6 (13)	61 (80)	6 (9)	30 (105)	49	12	32	1

NOTE. — The number of targeted, spectroscopically confirmed, and unclassified galaxies are given in Cols. (1)–(3). Values in parentheses denote the total targeted sample with each instrument. Confirmed galaxies that are neither  $\text{H}\alpha$ , [O III], [O II], or  $\text{Ly}\alpha$  are discussed in the text.

<sup>1</sup> Note that a subset of the samples were targeted with different instruments. These numbers account for overlapping targets.

<sup>2</sup> The FMOS reduction is not complete, as improvements for optimal spectral stacking and detection of weak emission lines have yet to be implemented. Thus, these confirmed numbers represent lower limits.

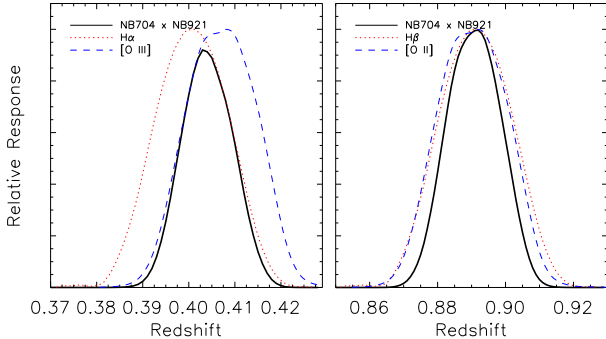


FIG. 4.— Redshift coverage for dual emitters. Dashed (blue) and dotted (red) lines show the NB704 and NB921 bandpasses, respectively. The product of the two filters is shown by the solid lines. The left (right) figure illustrates the [O III]– $\text{H}\alpha$  ([O II]– $\text{H}\beta$ ) combination for  $z \approx 0.40$  ( $z \approx 0.89$ ).

two NB filters for the [O III]– $\text{H}\alpha$  and [O II]– $\text{H}\beta$  combinations. Cross-matching a sample of 1421  $3\sigma$ -detected NB704 excess emitters (L07) with the NB921 emitting sample discussed, we found 241 dual NB704–NB921 emitters. These dual emitters are overlaid on Figure 3 as crosses. Among the dual emitters, 80 were spectroscopically targeted, and only nine of them have unidentified redshifts. Among the remaining 71 sources, 66 of them (93%) were  $\text{H}\alpha$  emitters. There are only two cases (3%) of dual [O II] and  $\text{H}\beta$  at  $z \approx 0.89$ . Since these lines are much weaker (by a factor of 5 to 10; see Hicks et al. 2002) than [O III] and  $\text{H}\alpha$  for typical star-forming galaxies at these redshifts, it is not a surprise that the majority of spectroscopically confirmed dual emitters are at  $z \sim 0.4$ .

### 3.2. Identifying [O II] Emitters

Rest-frame optical colors were previously used to distinguish the three most common redshifted emission lines, [O II], [O III], and  $\text{H}\alpha$ , entering into our narrow-band filters (L07). A small sample of spectroscopically confirmed sources is used to calibrate and optimize the broad-band color selection. With a much larger spectroscopic sample, we adopt an improved hybrid approach to select our [O II] samples for our analysis. First, spec- $z$ 's provide unambiguous classifications of NB excess emitters. For the NB921 (NB973) sample, 104 (32) candidates are definite [O II] emission-line galaxies. These spectroscopic confirmations represent  $\approx 10\%$  of the final [O II] samples. Next, we apply two-color photometry to select [O II] emitters. Illustrated in Figure 5 are the  $R_C - i'$  and  $i' - z'_{\text{cont}}$  colors for our excess emitters, where  $z'_{\text{cont}}$  is the “true” continuum at  $\sim 9200\text{\AA}$  after using the NB photometric measurements to remove contamination of

the nebular emission line into the  $z'$ :

$$z'_{\text{cont}} = z' + 2.5 \log \left( 1 + \frac{\text{EW}_{\text{obs}}}{955\text{\AA}} \right), \quad (6)$$

where  $955\text{\AA}$  is the FWHM of the  $z'$ -band filter. This is especially important since [O III] emitters with very large EWs will have unusually red  $i' - z'$  colors, which can be distorted enough to cross our color selection boundaries. The median differences in  $z'$  and  $z'_{\text{cont}}$  are 0.09 mag (NB921) and 0.14 mag (NB973), with average differences of 0.11 mag (NB921) and 0.24 mag (NB973), and can be as large as 1.25 mag (NB921) and 1.62 mag (NB973). The broad-band color choices were made in L07, and were designed to sample both sides of the Balmer/4000 $\text{\AA}$  break at  $z \sim 0.9$ , while for higher redshift, probing blueward of the break. In this figure, we have already excluded  $\text{H}\alpha$  emitters with our previous  $BR_C i'$  two-color selection (Ly et al. 2012). To select [O II] NB921 excess emitters with optical colors, we adopt:

$$R_C - i' \leq 0.05, \text{ or} \\ R_C - i' \leq 1.11(i' - z'_{\text{cont}}) - 0.01.$$

These color criteria are similar to those adopted in L07. With a larger spectroscopic sample, we determined that they only miss 1 of 100 (1%) spectroscopically identified [O II] NB921 emitters. Also, only 2 of 70 (3%) identified [O III] emitters meet the [O II] color selection. For selecting [O II] NB973 excess emitters, we adopt:

$$R_C - i' \leq 0.20, \text{ or} \\ R_C - i' \leq 0.45(i' - z'_{\text{cont}}) + 0.22.$$

Based on the above broad-band color selection, combined with our spectroscopic redshifts, we have identified 933 [O II] NB921 at  $z \approx 1.47$  and 328 NB973 at  $z \approx 1.62$ . We will now test these redshift determinations by comparing them with photometric redshifts.

### 3.3. Photometric Redshifts for NB Excess Emitters

While spectroscopy is not available for all galaxies, photo- $z$ 's can be determined from their individual SEDs. In a previous SDF study (Ly et al. 2011), we constructed a very large sample of  $\sim 200,000$  objects in SDF with photometric measurements in twenty bands: FUV, NUV,  $UBVR_C i' z' z_b z_r JHK$ , five narrow-band filters (NB704, NB711, NB816, NB921, and NB973), and two intermediate bands at  $\sim 6500\text{\AA}$ . By cross-matching our NB excess emitter catalogs against the ultra-deep SDF photometric catalog, we have full photometric measurements for 2132 of 2361 NB921 excess emitters and 1040 of 1243

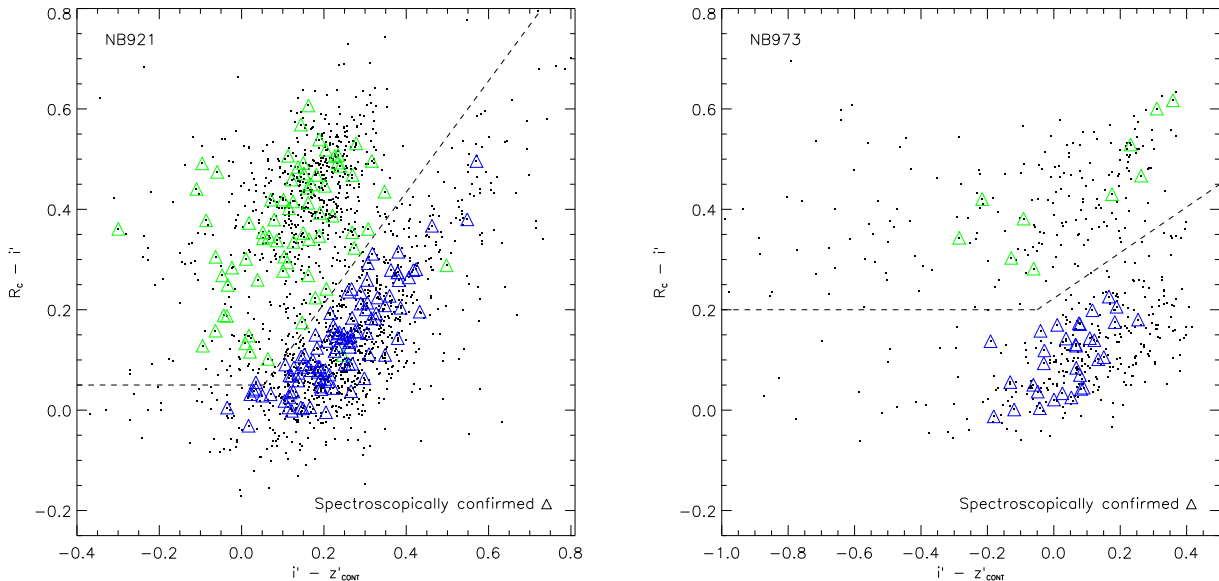


FIG. 5.—  $R_C - i'$  and  $i' - z'_{\text{cont}}$  colors for NB921 (left) and NB973 (right) emitters shown as black squares.  $H\alpha$  emitters, identified in Ly et al. (2012), have been excluded from this plot. Spectroscopically confirmed galaxies are shown as triangles with green and blue colors representing  $[O \text{ III}]$  and  $[O \text{ II}]$  emission entering the NB filter, respectively.

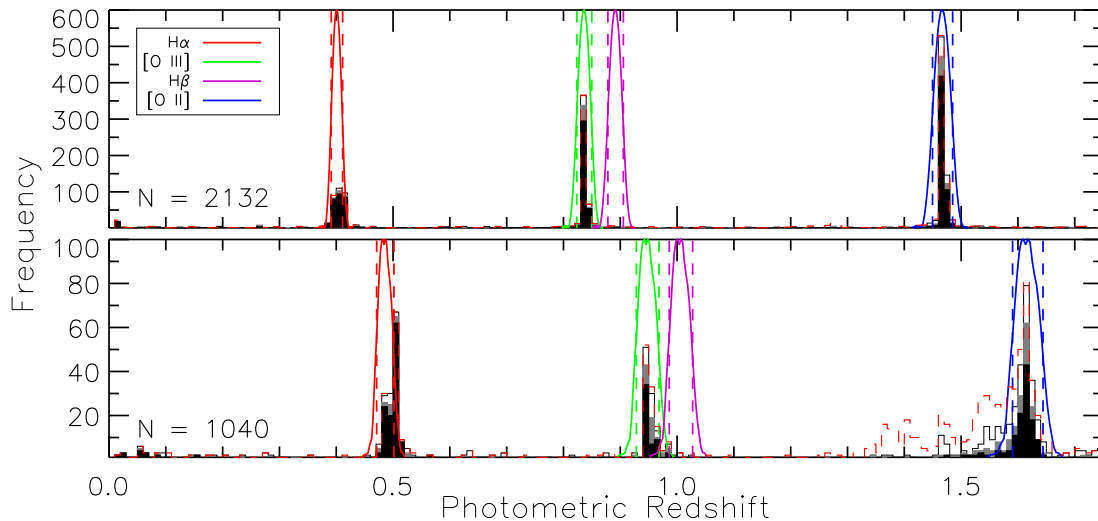


FIG. 6.— Photometric redshifts for NB921 (top) and NB973 emitters (bottom) derived from twenty-band photometry. Overlaid are the NB921 and NB973 filter profiles at the redshifts where  $H\alpha$  (red),  $[O \text{ III}]$  (green),  $H\beta$  (purple), and  $[O \text{ II}]$  (blue) enter the NB filters. Samples of NB excesses larger than  $3\sigma$ ,  $4\sigma$ , and  $5\sigma$  are shown by the solid black line, filled grey, and filled black histograms, respectively. The red histograms are intended to be compared against the black histograms to denote galaxies that have been flagged as interlopers with red  $i' - z'$  color (see Section 3). Vertical dashed lines show the FWHM of the filters.

NB973 excess emitters. The photo- $z$ 's for these sources were derived using the Easy and Accurate  $Z_{\text{phot}}$  from Yale (EAZY; Brammer et al. 2008). We illustrate these photo- $z$ 's in Figure 6, and compare them against our spectroscopic redshifts in Figure 7. There are good agreements between the photometric and spectroscopic redshifts: the rms of  $(z_{\text{phot}} - z_{\text{spec}})/(1 + z_{\text{spec}}) \equiv \frac{\Delta z}{1 + z_{\text{spec}}}$  is 0.0039 for NB921 and 0.0083 for NB973. This is not surprising, because the EAZY fitting routine includes emission lines, which are needed to match the observed broad- and narrow-band photometry. It appears that the photometric redshifts derived for  $H\alpha$  and  $[O \text{ II}]$  NB973 excess emitters are systematically off by  $\approx 1\%$ . The cause is unknown.

Not including NB filter measurements, the photo- $z$  distribution shows three peaks near the expected location for  $H\alpha$ ,  $[O \text{ III}]$ , and  $[O \text{ II}]$ . However, the photo- $z$  uncertainties are much larger, for example,  $[O \text{ II}]$  emitters have  $z_{\text{phot}}$ 's between 1.4 and 1.8.

We define a  $z_{\text{phot}}$  outlier as having  $\frac{\Delta z}{1 + z_{\text{spec}}} > 0.15$ . There are 56/250 (22.4%) and 15/91 (16.5%) failures for the NB921 and NB973 samples, respectively. As illustrated in Figure 8, the majority of these  $z_{\text{phot}}$  failures are associated with galaxies with high observed EWs. For example, in the NB921 sample, there are almost two dozen spectroscopically confirmed  $[O \text{ III}]$  emitters at  $z \approx 0.84$  with  $\text{EW}_{\text{obs}} \gtrsim 300\text{\AA}$ . All of them have incorrect photo-

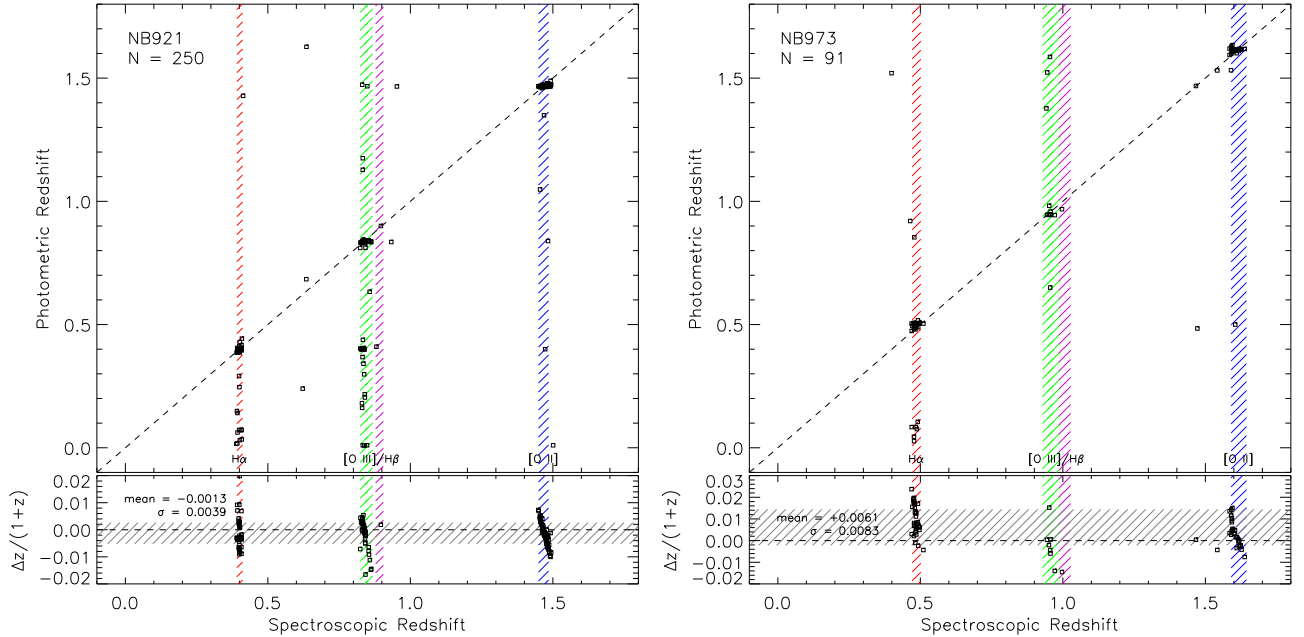


FIG. 7.— Comparisons between photometric and spectroscopic redshifts for NB921 (left) and NB973 (right) excess emitters. Shaded regions represent the redshift domain probed by the respective NB filter. One-to-one correspondence is shown by the dashed line. The bottom panels show the difference normalized by  $1 + z_{\text{spec}}$ :  $(z_{\text{phot}} - z_{\text{spec}})/(1 + z_{\text{spec}})$ .

$z$ 's, mostly  $z_{\text{phot}} \sim 0.4$ . We determined that the spectral templates used by EAZY do not allow for extremely strong [O III] emission compared to H $\alpha$  (i.e., [O III]/H $\alpha$  flux ratio greater than unity). As a result, EAZY finds a better fit by assuming that the large NB921 excess is due to H $\alpha$ . As L07 have shown, the [O III]/H $\alpha$  ratio from  $z \approx 0.4$  dual emitters were found to be on average, unity. EAZY will need to be revised to account for the recently observed fact that star-forming galaxies at high- $z$  have very large [O III]/H $\alpha$  ratios, perhaps due to low gas-phase metallicity (Atek et al. 2011). A similar problem occurs for the spectroscopically confirmed H $\alpha$  emitters where they are placed at  $z \sim 0.1$ , a redshift which puts H $\alpha$  in the NB704 filter. However, the NB704 excess is in fact due to [O III]. This problem occurs when the observed H $\alpha$ + [N II] EW is above 100Å.

Other studies have examined photo- $z$ 's for emission-line galaxies and found less catastrophic failures. For example, Xia et al. (2011) found very few catastrophic failures between photometric and grism redshifts. However, it is not clear what fraction of their sample targeted high EWs, so a direct comparison is not possible. We note that there are fortunately very few [O II] NB921 failures. Only 3 of 36 (8%) have incorrect  $z_{\text{phot}}$ . The higher success for the [O II] selection is because, blueward of 3600Å, the SED is simple: no additional emission lines enter our optical bands, and the Balmer/4000Å break is shifted past 9000Å.

We note that among the photo- $z$  sample, 77% and 58% have photo- $z$ 's consistent with having [O II] entering the NB921 and NB973 filters, respectively. These numbers should be taken as lower limits to the real success of the [O II] color selection, because many of the apparently discrepant photometric redshifts were highly uncertain, based on rather limited multi-band data. If we restrict our consideration to only the most robustly determined photo- $z$ 's, we would find an even higher success rate of

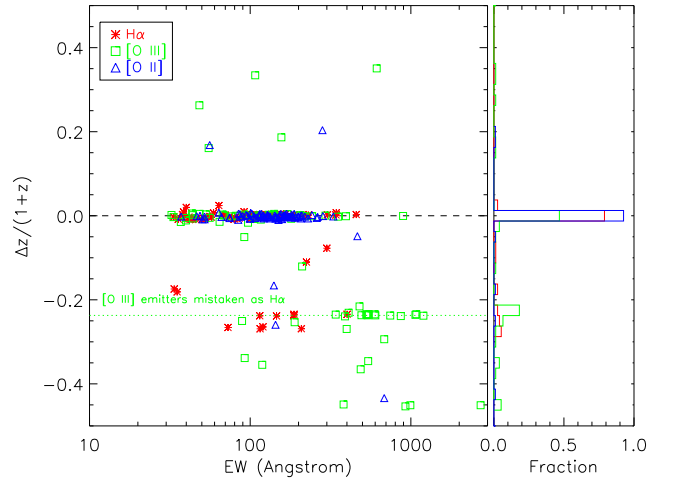


FIG. 8.— Photometric redshift accuracy,  $\frac{\Delta z}{1+z_{\text{spec}}}$ , as a function of NB921 observed EW. H $\alpha$ , [O III], and [O II] emitters are denoted as red asterisks, green squares, and blue triangles, respectively. A significant number of the  $z = 0.84$  [O III] emitters have incorrect photo- $z$ 's due to high [O III]/H $\alpha$  flux ratios, which are not considered in EAZY spectral templates. These galaxies, with high [O III] EWs, are believed to have low gas metallicities.

identifying [O II]-emitting galaxies.

## 4. RESULTS

### 4.1. [O II] Equivalent Width Distributions

Figure 9 shows the distributions of the rest-frame [O II] EW ( $EW_0$ ), for galaxies detected at  $\geq 3\sigma$  in the NB921 and the NB973 filters. The distribution for NB921 emitters further emphasizes the excellent sensitivity our NB921 imaging provides even for galaxies with relatively weak [O II] lines, with  $EW_0 \sim 15\text{\AA}$ . Although our ability to detect [O II] falls off for  $EW_0$ 's below  $\sim 25\text{\AA}$ , the broad peak of the observed detections around an  $EW_0$  of 43Å suggests that our NB921 survey misses relatively



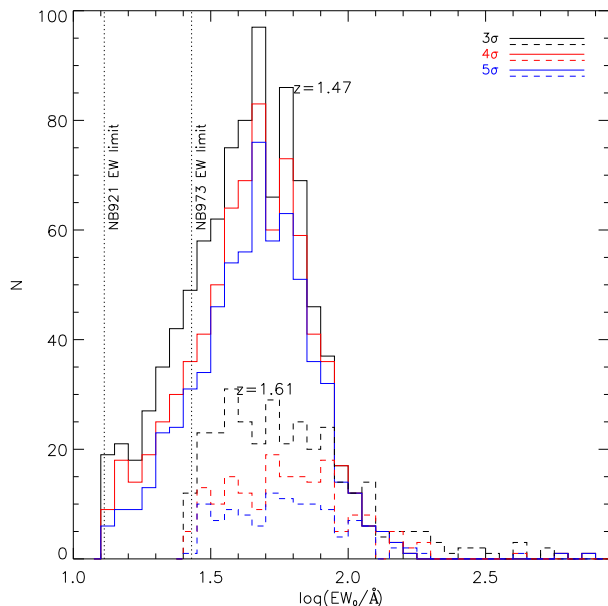


FIG. 9.— Rest-frame [O II] EW distributions for our NB921 (solid line) and NB973 (dashed line) samples. The dotted lines indicate the EW selection limits of our surveys. Also shown are the distributions when the samples are limited to NB excesses of  $> 4\sigma$  (red) and  $> 5\sigma$  (blue), analogous to Figure 6.

few galaxies, since most of them have EWs larger than our sensitivity limit. One piece of evidence that supports this is the comparison of the EW distributions with more conservative NB excesses limits ( $4\sigma$  and  $5\sigma$ ; see Figure 9). In these cases, the distributions still have the same shape: peaking at the same EW with the lower EW slope unchanged. If there was a significant number of 15–25 Å [O II] emitters detectable at  $3\text{--}5\sigma$ , we would see a more rapid decline prior to our EW selection limits.

Recently, Kornei et al. (2012) also investigated the [O II] EW of star-forming galaxies at somewhat lower redshifts of  $z = 0.7\text{--}1.3$ . They find a similar median [O II] EW<sub>0</sub> of 45 Å, and also find a similar decline towards lower EWs. This result provides further independent support for our claim that our NB921 survey misses few galaxies in the redshift range for [O II], because that line is nearly always present.

In addition, another NB survey that examined the H $\alpha$  EWs at  $z = 2.2$  finds that the H $\alpha$  EW<sub>0</sub> distribution peaks at 140 Å,  $\approx 120\text{Å}$  above the survey limit, and intrinsically falls off rapidly towards lower EWs (Lee et al. 2012).

#### 4.2. Comparison of [O II] and UV Continuum Luminosities

For galaxies at any appreciable redshifts ( $z > 0.5$ ), the most common observable used to estimate their current star formation rates (SFRs) is their UV continuum emission. This works because in all but the oldest stellar populations, the far-UV continuum (1500 Å rest wavelength) should be dominated by the hottest, and thus shortest-lived, main-sequence stars (O and B types). Since the hottest of these produce most of the ionizing photons in a galaxy, it is expected that as the rate of current star formation increases, so does the UV continuum as well as the emission line luminosity from H II regions. The “gold standard” measure used to count ionizing photons is the H $\alpha$  recombination line, but this is redshifted beyond the

sensitivity of the best CCD spectrographs at  $z \sim 0.5$ . To study higher redshifts, secondary emission lines from ionized gas have been explored at shorter wavelengths. The most “popular back-up” indicator of SFR is the luminosity of the [O II] doublet.

Figure 10 shows the *observed* luminosities of the [O II] emission line as a function of the *observed* far-UV continuum at 1500 Å. The solid line shows the least-squares regression after binning our data in  $L(1500)$ :  $\log L(\text{OII}) = 16.23 + (0.89 \pm 0.22) \log L(1500)$ . Here,  $L(1500)$  is determined directly from the  $U$ -band photometry

$$\log \left[ \frac{L(1500)}{\text{erg/s/Hz}} \right] = \frac{(M_U + 48.6)}{-2.5} + 40.08, \quad (7)$$

where  $M_U = U + 2.5 \log(1+z) - 5 \log(d_L/10 \text{ pc})$ , and  $d_L$  is the luminosity distance,  $1.06 \times 10^4 \text{ Mpc}$  for  $z = 1.47$ . And the [O II] luminosity is determined from narrow-band and broad-band measurements:

$$L(\text{OII}) = \Delta\text{NB} \left[ \frac{f_{\lambda,\text{NB}} - f_{\lambda,z}}{1 - (\Delta\text{NB}/\Delta z)} \right]. \quad (8)$$

In fitting the  $L(1500)\text{--}L([\text{O II}])$  relation, we have excluded measurements below  $\log L(1500) = 27.75$ , since the [O II] measurements are biased against galaxies that are fainter than the current [O II] depth permitted by our NB imaging.

Both of these observables have been calibrated to predict the SFR of a galaxy (Kennicutt 1998), if the quantities can be corrected for interstellar extinction. Kennicutt (1998)’s SFR relation for  $L(\text{OII})$  is based on the calibration for H $\alpha$ . In his sample of nearby spiral galaxies, he estimated  $L(\text{OII}) = 0.45 L(\text{H}\alpha)$ .<sup>12</sup> He recommends an average H $\alpha$  extinction correction factor of 2.5 (Kennicutt 1992). Thus, we have

$$\text{SFR} = 2.0 \times 10^{-41} L(\text{OII}) \left[ \frac{L(\text{H}\alpha)}{L(\text{OII})} \right]. \quad (9)$$

For a Salpeter (1955) (hereafter Salpeter) initial mass function (IMF), the far-UV continuum and SFR are also related by a simple linear proportionality:  $\text{SFR} = 1.4 \times 10^{-28} L(1500) \times 10^{0.4A(1500)}$ , where  $A(1500) = 1.37 \text{ mag}$  assuming a Calzetti et al. (2000) dust curve with  $A(\text{H}\alpha) = 1 \text{ mag}$  and  $E(B - V)_{\text{star}} = 0.44 E(B - V)_{\text{gas}}$ . If we require that both observable diagnostics must yield the same SFRs, then we would expect a simple linear relation between observed  $L(\text{OII})$  and  $L(1500)$ :

$$L(\text{OII}) = 2.5 \times 10^{13} L(1500) \frac{L(\text{OII})}{L(\text{H}\alpha)}. \quad (10)$$

This linear relation is shown in Figure 10 for two values of the observed [O II]/H $\alpha$  flux ratio, 0.5 and 1.0. This comparison suggests that, if the Kennicutt (1998)’s SFR relations are correct for  $L(1500)$  and for  $L(\text{H}\alpha)$ , then our data indicate that the [O II]/H $\alpha$  flux ratio is typically 0.75 for the majority of our sample. Sobral et al. (2012) also compared the [O II] and H $\alpha$  flux ratio at the same redshift and found a typical ratio of 0.4–0.8. For a subset of our sample with high UV luminosities, the

<sup>12</sup>  $L(\text{OII})$  and  $L(\text{H}\alpha)$  are observed (i.e., not de-reddened).



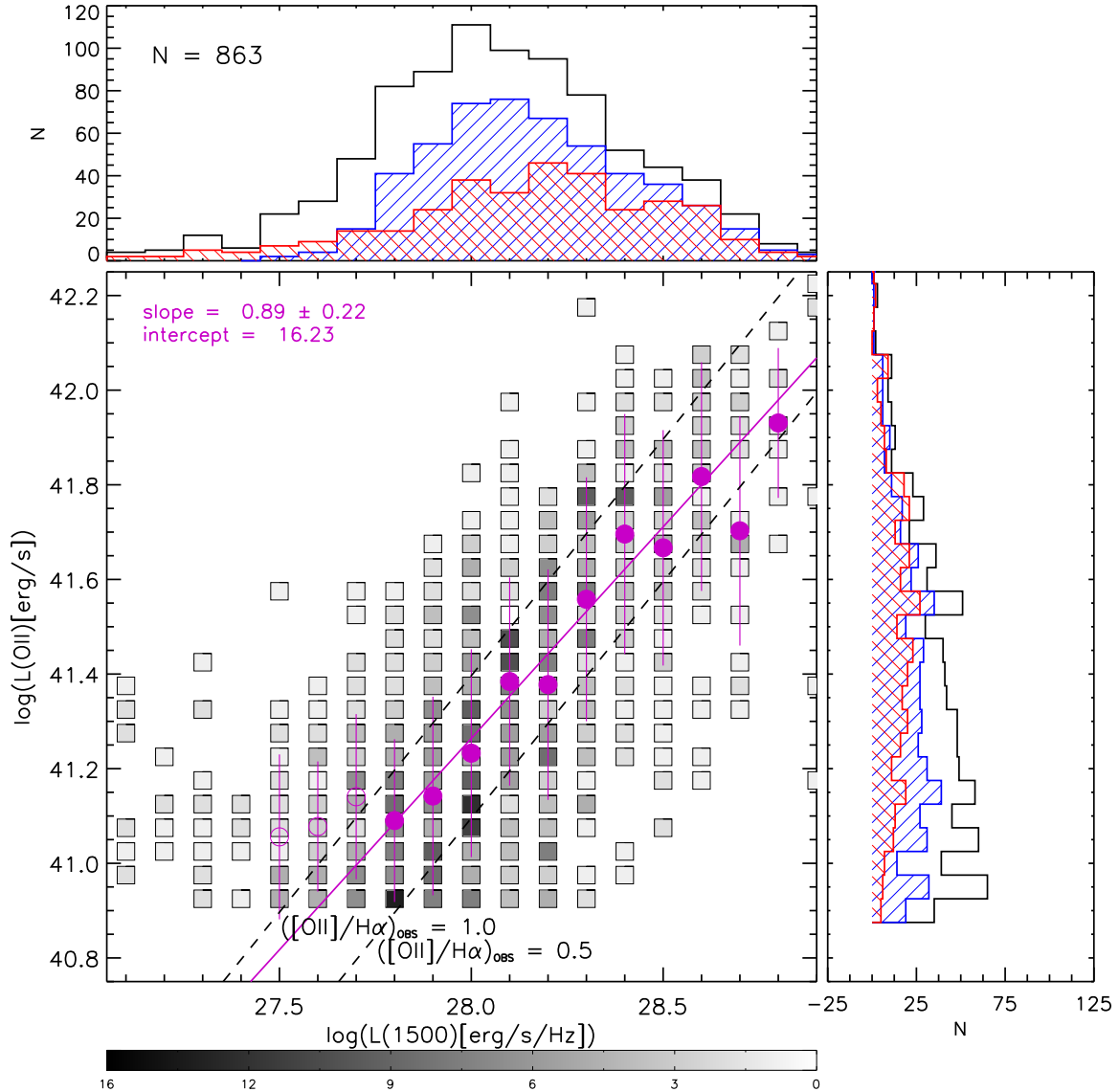


FIG. 10.— Observed [O II] and UV luminosities of  $z = 1.47$  [O II] emitters. The greyscale represents the density of points in each bin. Purple filled circles show the median at each UV luminosity bin with error bars representing 68% of the [O II] measurements. Overlaid as dashed lines are the cases where the observed [O II]/ $H\alpha$  flux ratio is 0.5 and 1.0 following Equation 10. The histograms collapse the distributions into one dimension with blue and red colors indicating those [O II] emitters meeting the BX/BM and sBzK selections (discussed further in Sections 4.5.1–4.5.2), respectively.

[O II]/ $H\alpha$  ratio decreases towards 0.5. This is consistent with the same decline in [O II]/ $H\alpha$  flux ratio with blue stellar luminosity found by Jansen et al. (2001) in local galaxies. Illustrated in Figure 10, the scatter of the [O II] luminosity relative to the UV luminosity suggests that [O II] can be used as a SFR indicator with a reliability of  $\sigma = 0.23$  dex.

#### 4.3. Average Spectral Energy Distributions of [O II]-Emitting Galaxies

We have combined our multi-wavelength photometry from hundreds of [O II]-emitting galaxies to construct representative broad-band SEDs. We limit our results to the NB921 sample, since the results are better constrained with the larger and deeper sample. Our filters,  $U$  through IRAC 1 and 2 (Fazio et al. 2004), span rest-frame  $1500\text{\AA}$ – $1.8\mu\text{m}$ , more than ten times the spectral

coverage that was possible with the Suprime-Cam data alone, that was used by L07.

In Figure 11 we show the median SEDs of  $z = 1.47$  [O II] emitters, dividing the sample between high- and low-equivalent width of [O II] emission (greater or less than  $106\text{\AA}$ ) and between low and high [O II] flux (above and below  $1.49 \times 10^{-17} \text{ erg s}^{-1} \text{ cm}^{-2}$ ). For comparative purposes, all SEDs are normalized to 23.0 mag in the  $i'$  band. The error bars show the range encompassing 68% of the data in each waveband.

The average  $U$ -to- $i'$  photometry (corresponding roughly to rest wavelengths between  $1500$  and  $3300\text{\AA}$ ) can be approximated by a power law ( $F_\nu \propto \nu^\alpha$ ) with  $\alpha = -0.64$ , except for a marginal but systematic dip in the intermediate  $6000\text{\AA}$  filter, which might possibly be attributed to the broad  $2200\text{\AA}$  peak in the interstellar reddening law. On the red side of the  $i'$  band, the SEDs

rise much more rapidly, due to the Balmer and Ca II H and K breaks with an average  $i' - K$  color of 1.2 mag. Redward of the jumps, the rest-frame optical continuum is relatively flat. This is supported by the IRAC [3.6] and [4.5] photometry. We note also that at this redshift of  $z = 1.47$ , [O III] and  $H\beta$  enter the  $J$ -band, and thus can alter these colors if these emission-line EWs are extremely high, as seen in other surveys (e.g., Atek et al. 2011). Indeed, if we compare the average  $J$  flux of the high-EW galaxies to a typical model SED going through the surrounding filters, it appears to be a few tenths of a magnitude brighter. This is attributable to the contamination from the [O III] and  $H\beta$  lines.

As found by L07, the average SED of the high-EW sub-sample is systematically bluer than of the moderate-EW subset: the observed  $\langle U - i' \rangle$  and  $\langle i' - K \rangle$  colors are  $0.43 \pm 0.27$  and  $1.13 \pm 0.35$  and  $0.58 \pm 0.32$  and  $1.28 \pm 0.50$  for the high- and low-EW sub-samples, respectively. This is reasonable, since the former galaxies, with specific SFRs several times higher, should have a larger fraction of younger, blue stars. We also find that galaxies with higher [O II] emission-line fluxes are found to be redder than those with weaker [O II] flux. We argue that this is due to a selection effect that more massive galaxies tend to be redder will have higher SFRs and thus higher [O II] fluxes. We next quantify these trends with fits of model stellar populations to the SEDs.

#### 4.4. Stellar Populations from SED Modeling

We modeled the fifteen-band SEDs of our [O II] emitters to derive stellar masses, SFRs, dust reddening ( $A_V$ 's), and stellar ages. At  $z \sim 1.5$ , the data span rest-frame 600Å–8800Å. The spectral synthesis models are discussed further in Ly et al. (2011). In brief, we use the IDL-based code, Fitting and Assessment of Synthetic Templates (FAST; Kriek et al. 2009), with exponentially declining  $\tau$  star-formation history models from Bruzual & Charlot (2003). We adopt a Salpeter IMF, and dust attenuation follows the Calzetti et al. (2000) reddening formalism. A Chabrier (2003) IMF was also considered; however, the resulting  $\chi^2$  fits (ages,  $\tau$ 's, and  $A_V$ 's) were no different from those determined using a Salpeter IMF. The only difference was a lower stellar mass and SFR by 0.25 dex (a factor of 1.8), which is expected due to the smaller proportion of low-mass stars. Therefore, we adopt the Salpeter IMF for the remainder of this paper. To correct for neutral hydrogen intergalactic medium absorption, we follow the prescriptions described in Madau (1995).

The grid of models consists of  $\log(\tau/\text{yr}) = 7.0, 8.0, 9.0,$  and  $10.0$ . These  $\tau$  values were selected to include a bursty, intermediate, and roughly constant star-formation history. In addition to the star-formation history, the grid of models spans a range of  $\log(\text{age}/\text{yr})$ , between 6.0 and up to the age of the universe at a given redshift (in increments of 0.1 dex), and dust extinction with  $A_V = 0.0$ –3.0 mag with 0.1 mag increments. We only consider solar metallicity models, since distinguishing different metallicities is nearly impossible with broad-band SED fitting (see e.g., Pforr et al. 2012).

In these fits, the redshifts are accurately fixed, either from the spectroscopic values when available, or from the presence of [O II] in the NB bandpass ( $z = 1.467$

or  $z = 1.617$ ). Since these spectral synthesis models do not include nebular emission lines, we correct the  $z'$ -band measured fluxes to remove the [O II] emission contribution to these filters. We note that by having the photometry as is, the stellar masses were higher by 0.2 dex, the stellar ages were older by 0.1 dex, and the SFRs were lower by 0.3 dex.

In Figure 12, we illustrate the stellar masses and ages for 863  $z \approx 1.47$  [O II] emitters. We find that these [O II] emitters span 2 dex in stellar age with a median of  $\sim 100$  Myr and 3 dex in stellar mass with a median of  $3 \times 10^9 M_\odot$ . In modeling the broad-band SED, there is a known degeneracy between the fitted stellar age and dust reddening in describing the overall spectral slope, particularly in the UV. In particular, one can make galaxies appear younger but with significant dust and vice versa. We caution that fits with very young stellar populations ( $\lesssim 10$  Myr) may not be reliable because they also give very large extinction ( $A_V = 1$ –3 mag).

We find that the galaxies with observed [O II] EW above 106Å have on average a factor of two less stellar mass than the low-EW galaxies. In addition, galaxies with [O II] fluxes above  $1.49 \times 10^{-17}$  erg s $^{-1}$  cm $^{-2}$  are more massive by a factor of 5. These results are consistent with the average SED results discussed in Section 4.3 since more (less) massive galaxies are typically expected to have redder (bluer) colors.

#### 4.5. Testing Color-Selection Techniques at $z > 1$

The two techniques commonly used to select star-forming galaxies at redshifts of 1–3 are the “BX/BM” (Adelberger et al. 2004) and “sBzK” (Franx et al. 2003; Daddi et al. 2004) methods. The former approach, analogous to the Lyman break method (Steidel & Hamilton 1992), finds young galaxies with strong star formation and moderately red  $U_n - G$  color due to the Lyman continuum break beginning to enter into the  $U_n$  filter. The latter method is intended to identify  $z \gtrsim 1.4$  galaxies when the Balmer/4000Å break occurs between  $z'$  and  $K$ . Because of the need for  $K$ -band data, the BzK method is generally biased towards more massive galaxies. These methods were developed to help “fill” the historically known “redshift desert” where wide-field deep UV imaging to identify  $z \sim 1.5$  Lyman break galaxies was not available until more recently (Ly et al. 2009; Hathi et al. 2010; Oesch et al. 2010; Basu-Zych et al. 2011; Habertzettl et al. 2012). These color selections and their respective samples identified for the SDF are discussed in Ly et al. (2011), where they illustrated that a wide range of the stellar populations of galaxies at  $z \gtrsim 1$  is probed by combining these two complementary methods.

With deep multi-wavelength coverage for the SDF, we examine which of our [O II] emitters are classified as UV-selected “BX/BM” galaxies and/or NIR-selected BzK galaxies.

Since we argued above that *most* galaxies at  $z = 1.47$  have detectable [O II] emission lines, we can use our large NB samples to test the completeness of the two main broad-band color search methods available at the same redshift. We find that both suffer from some incompleteness, which is mostly eliminated by combining the two methods.

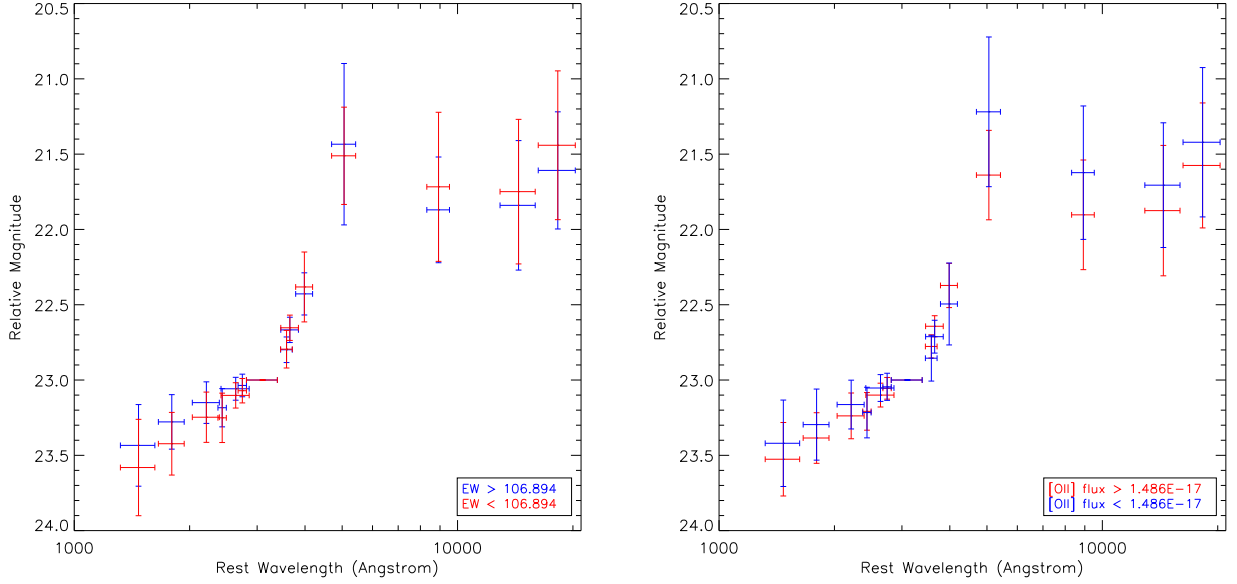


FIG. 11.— Broad-band SEDs for NB921 [O II] emitters constructed by binning the sample in EW (left) and [O II] emission-line flux (right). Each SED is constructed from roughly 350 galaxies where the sub-samples are constructed above and below the median EW and [O II] flux. Error bars represent 68% of the sub-samples, and blue and red colors denote the samples with bluer and redder rest-frame UV colors.

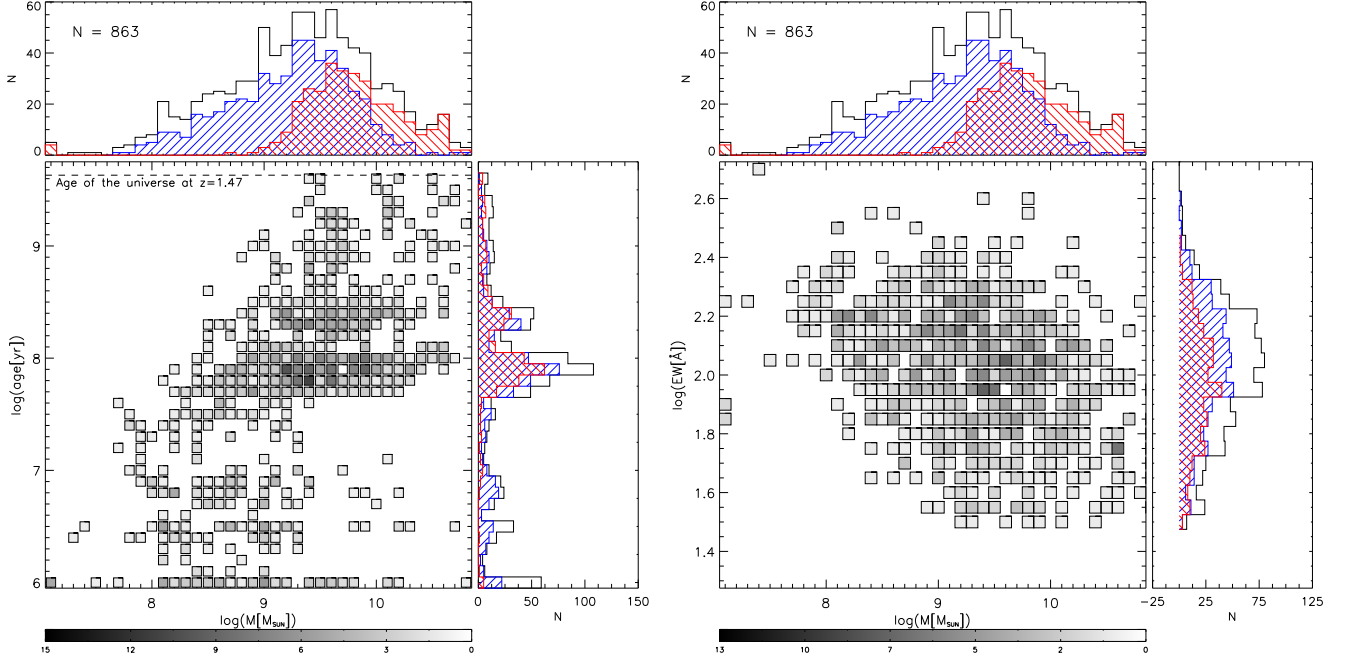


FIG. 12.— Stellar ages, stellar masses, and [O II] observed EWs for the  $z = 1.47$  [O II] NB921 emitters. These quantities were derived from SED modeled fits that assumed a Salpeter IMF, an exponentially declining star-formation history, and Calzetti et al. (2000) internal dust reddening. The histograms collapse the distributions into one dimension with blue and red colors indicating those [O II] emitters meeting the BX/BM and sBzK selections, respectively.

#### 4.5.1. The BX/BM Sample

Figure 13(a) shows the  $U_n - G$  and  $G - \mathcal{R}$  colors for both of [O II] emitting samples. Since the SDF does not have these exact filters, we derive these colors by using a combination of the  $UBVR_Ci'$  filters that are measured. The color transformation was determined by using stellar population synthesis models representative of UV luminous galaxies (Ly et al. 2011), and consists of:

$$U_n = U, \quad (11)$$

$$G = BV \equiv -2.5 \log \left[ \frac{x_1 f_B + (1 - x_1) f_V}{3630 \mu\text{Jy}} \right], \quad \text{and} \quad (12)$$

$$\mathcal{R} = R_C i' \equiv -2.5 \log \left[ \frac{x_2 f_R + (1 - x_2) f_{i'}}{3630 \mu\text{Jy}} \right]. \quad (13)$$

Here,  $f_X$  is the flux density per unit frequency ( $\text{erg s}^{-1} \text{cm}^{-2} \text{Hz}^{-1}$ ) in band “X”, and  $x_1 = 0.314$  and  $x_2 = 0.207$ , as discussed in Ly et al. (2011).

Limiting our consideration to  $R_C \leq 25.5$ , the typical depth adopted by past and current BX/BM surveys, we

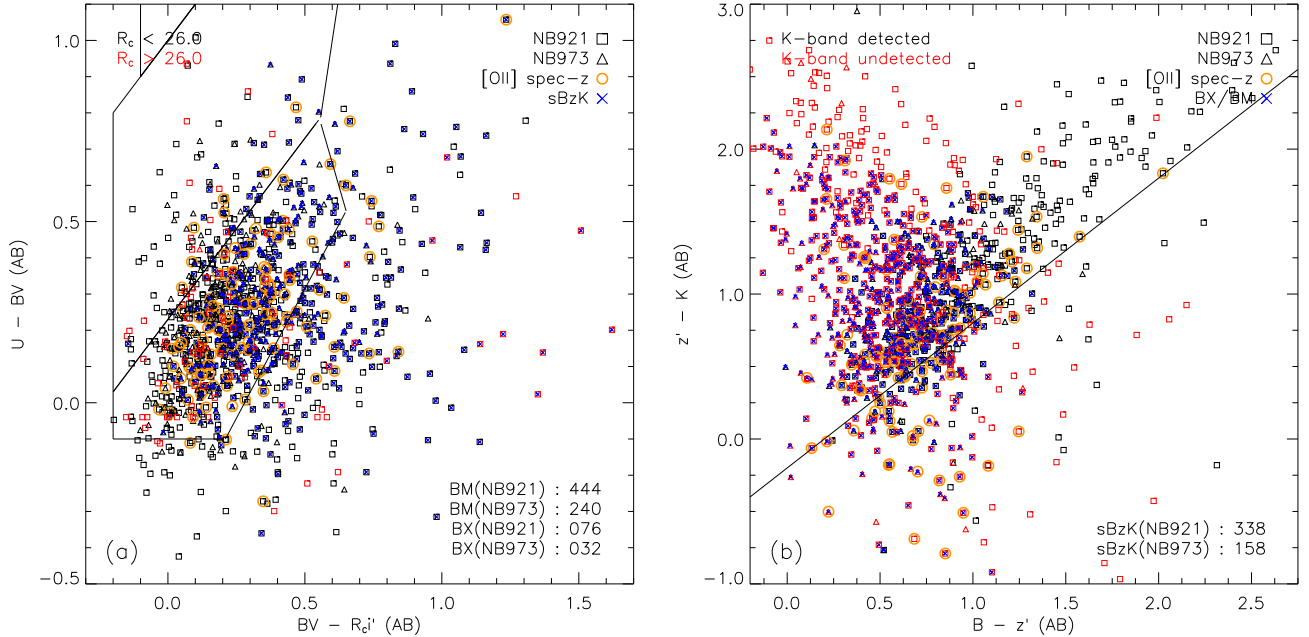


FIG. 13.— (a)  $U - BV$  and  $BV - R_C'$  colors for [O II] emitters. Red symbols denote sources fainter than  $R_C = 26.0$ . BM, BX, and  $U$ -dropout galaxies are selected by the three regions defined by the solid lines (from bottom to top, respectively). Most galaxies are classified as BM, which is expected for  $z = 1.47$  and  $1.62$ . (b)  $B - z'$  and  $z' - K$  colors for [O II] emitters. Red symbols identify sources that are undetected in the  $K$ -band at the  $3\sigma$  level (upper limits on  $z' - K$ ). Star-forming BzK galaxies are classified as those lying above the diagonal line. Both panels show blue crosses to denote the galaxy population selected by the other method. The NB921 and NB973 [O II] samples are distinguished by squares and triangles, respectively. Spectroscopically confirmed [O II] emitters are shown as orange circles.

find for the full  $z = 1.47$  [O II] sample that 47% are BX or BM. Likewise, 82% of the  $z = 1.62$  [O II] emitters are either BX or BM. We summarize these statistics, as well as those for  $R_C \leq 26.0$ , in Table 2.

#### 4.5.2. The sBzK Sample

The  $B - z'$  and  $z' - K$  colors for the [O II] emitters are illustrated in Figure 13(b). Since the SDF is not fully covered (80%) with UKIRT/ $K$ -band observations to a  $3\sigma$  sensitive depth of 23.9 mag, we limit the sample of [O II] emitters to those that are in the sensitive region. Among the 863  $z = 1.47$  (313  $z = 1.61$ ) [O II] emitters, 750 (264) sources are located within the sensitive region. Requiring a  $3\sigma$  detection in  $K$ , the samples are further limited to 402 (NB921) and 174 (NB973). Daddi et al. (2004) defines star-forming BzK (sBzK) as galaxies with  $z' - K \geq (B - z) - 0.2$ . This yields 84% of [O II] NB921 and 91% of [O II] NB973 emitters as sBzK galaxies. None of these [O II] emitters have colors that would classify them as passive BzK. Thus both color methods, especially BzK, work very well to find emission-line galaxies.

We emphasize that 80 of 576 (14%)  $K$ -band detected [O II] emitters have blue  $z' - K$  colors preventing them from being selected as sBzKs. As illustrated in Figure 13(b), a large fraction of these has been spectroscopically confirmed to be at  $z = 1.47$  or  $z = 1.62$ . Lee et al. (2012) have also shown that for a sample of  $z = 2.2$  H $\alpha$  emitters, 8% are also missed because of their blue  $z' - K$  colors. They argued that the sBzK selection fails to identify galaxies with relatively younger stellar population due to little or no Balmer break. Barger et al. (2008) also examined the BzK selection with a large spectroscopic sample and find that the sBzK selection is effective at identifying high redshift galaxies, but may suffer from significant (33%) contamination from  $z < 1.4$

interlopers.

#### 4.5.3. Stellar Population Characteristics of Color-Selected Galaxies

To illustrate the diversity of the [O II] sample and the selection biases associated with the BX/BM and sBzK techniques, we plot their distributions of stellar masses, ages, and [O II] EW in Figure 12. It is apparent that the sBzK selection (shown in red) is well designed to identify almost all of the massive [O II] emitters, but becomes seriously incomplete below  $3 \times 10^9 M_\odot$ . This incompleteness is caused by the current depth in the  $K$ -band. By contrast, the BX/BM selection (shown in blue), succeeds at identifying most of the low-mass galaxies, but misses about half of the massive population. In addition, we present the first determination of [O II] EW distributions for large representative samples of BX/BM and sBzK galaxies. The BX/BM sample is skewed towards higher observed EWs (average of 105Å) compared to sBzKs (average of 91Å).

We illustrate in Figure 14(a) the observed [O II] emission-line EW as a function of  $R_C - z'$ . It is clear that the BX/BM and sBzK techniques are complementary by identifying the bluest and reddest galaxies, respectively. Roughly 25% of the [O II] emitters are identified using both color selections, while 34% and 20% are identified by only the BX/BM and sBzK selections, respectively. Figure 14(a) also shows that  $\sim 20\%$  (154/750) of the [O II] sample is not identified by either method. These galaxies are generally of lower luminosity where 43% of them are fainter than  $R_C = 26.0$  mag and 84% are undetected (at  $3\sigma$ ) in  $K$ . These galaxies have typical limits on their stellar mass of  $\sim 3 \times 10^8 M_\odot$ . We note that the [O II] emitters galaxies with  $R_C < 26.0$  but which still miss the BX/BM selection have typical stellar masses of  $2 \times 10^9$



TABLE 2  
 SUMMARY OF BX/BM AND sBzK RESULTS FOR [O II] EMITTERS

Filter (1)	$N$ (2)	$N_{\text{phot}}$ (3)	$N(R \leq 25.5)$ (4)	$N(R \leq 26.0)$ (5)	UV( $R \leq 25.5$ ) (6)	UV( $R \leq 26.0$ ) (7)	$N(\text{K-det})$ (8)	$N(\text{sBzK})$ (9)	$N(\text{Either})$ (10)
NB921	933	863 92.5%	585 67.8%	741 85.9%	406 47.0%	520 60.3%	...	...	...
...	(814)	(750 92.1%)	(505 67.3%)	(641 85.5%)	(348 46.4%)	(446 59.5%)	(402 53.6%)	(338 45.1%)	(596 79.5%)
NB973	328	313 95.4%	286 91.4%	307 98.1%	255 81.5%	272 86.9%	...	...	...
...	(278)	(264 95.0%)	(238 90.2%)	(258 97.7%)	(210 79.5%)	(226 85.6%)	(174 65.9%)	(158 59.8%)	(248 93.9%)

NOTE. — Values reported in parentheses refer those sources that fall in the sensitive  $K$ -band region (“K-det”). Except for those reported in Col. (3), all percentages are relative to  $N_{\text{phot}}$ . In Cols.(6)–(7), “UV” refers to the combination of “BX” and “BM” selections.

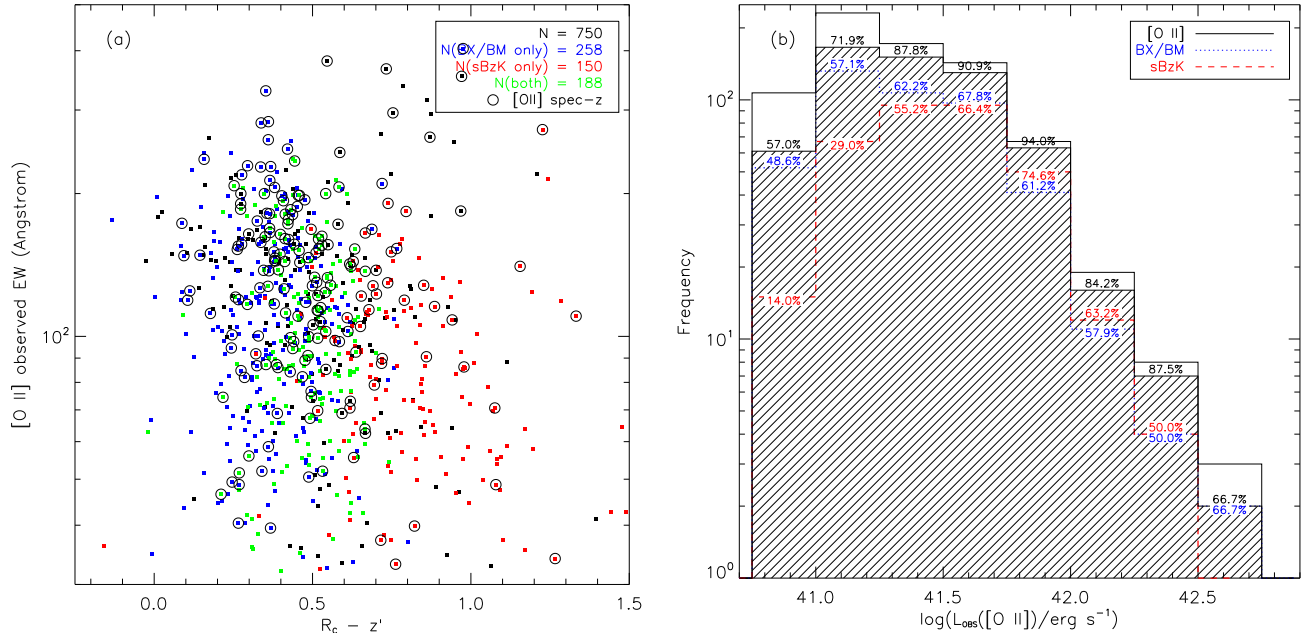


FIG. 14.— (a) [O II] observed EW as a function of  $R_C - z'$  color for NB921 emitters. [O II] emitters that are selected purely as “BX/BM” ( $R_C < 26.0$  mag) and sBzK are shown as blue and red squares, respectively. Those identified using both color selection techniques are shown as green squares, and those that do not meet both selections are shown as black squares. Spectroscopically confirmed [O II] emitters are shown as black circles. (b) The probability distribution of [O II] observed luminosity, as shown by the solid black line. The red dashed line illustrates the distribution for [O II] sBzK galaxies. Likewise, the blue dotted line shows the [O II] BX/BM galaxies. The combination of both method is shown by the shaded histogram. Percentages are reported relative to the full [O II] sample.

$M_{\odot}$ , which is 0.25 dex more (0.86 less) massive than the BX/BM (sBzK). This suggests that a subset of intermediate mass star-forming galaxies are missed by color selections.

Finally the distribution of [O II] luminosity for the sBzK and BX/BM samples are shown in Figure 14(b) where it illustrates that either of these color selections will miss 40%–50% of the [O II] sample. Even combining both methods, roughly 20% of the faintest [O II] emitters are missed.

## 5. CONCLUSIONS

Using deep NB imaging with Suprime-Cam, we identified  $\sim 1,300$  [O II] emitting galaxies at  $z=1.5$ – $1.6$ . Follow-up optical and near-infrared spectroscopy confirmed that the two-color selection of [O II] emitters is highly reliable: Only 1% of NB921 [O II] emitters appeared to be missed while 3% of  $z = 0.84$  [O III] emitters contaminate the [O II] NB921 color selection. Our survey has investigated the properties of [O II]-emitting galaxies. We find:

1. The average rest-frame [O II] EW of our  $z = 1.47$  sample is  $45\text{\AA}$ , consistent with another study at

$z > 0.7$ . The EW distribution declines gradually from the peak towards lower EWs, suggesting that very few  $z \sim 1.5$  galaxies lack [O II] emission.

2. We compared the observed [O II] and UV luminosities and find a strong correlation with  $\log L(\text{O II}) \propto (0.89 \pm 0.22) \log L(1500)$ . The observed scatter (0.23 dex) of individual [O II] measurements against the UV luminosity suggests that the [O II] luminosity can be considered as a coarse SFR indicator.
3. We constructed multi-band SEDs (rest-frame  $1500\text{\AA}$ – $1.8\mu\text{m}$ ), and find that higher EW galaxies have slightly bluer colors compared to lower EW galaxies.
4. We fitted the SEDs with exponentially declining “ $\tau$ ” models, and find a median stellar ages of 100 Myr with 13% of the sample older than 500 Myr. The stellar masses are typically  $10^{9.5 \pm 0.6} M_{\odot}$ .
5. We find that [O II] emission is present in the full census of galaxies, from massive red systems (found by sBzK) to smaller, star-bursting systems (found by BX/BM). With the sensitivity that we achieved

in the NB921 filter, we find that 154 ( $\approx 20\%$ )  $z = 1.47$  [O II] emitters are not identified with BzK or BX/BM because they are too faint (i.e., stellar mass limits of  $\sim 3 \times 10^8 M_{\odot}$ ). A subset of these unidentified galaxies that are bright enough to satisfy the BX/BM magnitude limit ( $R_C = 26.0$ ) have intermediate stellar masses ( $2 \times 10^9 M_{\odot}$ ) compared to the BX/BM and sBzK samples, and suggest that some intermediate mass galaxies are currently missed by commonly used high- $z$  color selections.

We thank Nelson Caldwell with help on designing Hectospec fiber configurations, Richard Cool for addi-

tional help using the MMT/Hectospec HSRED reduction pipeline, and Ryosuke Goto for assistance in the FMOS observations. The authors wish to recognize and acknowledge the very significant cultural role that the summit of Mauna Kea has always had within the indigenous Hawaiian community. We are most fortunate to have the opportunity to conduct observations from this mountain.

*Facilities:* Subaru (Suprime-Cam, FOCAS, FMOS), MMT (Hectospec), Keck (DEIMOS), *GALEX*, Mayall (MOSAIC, NEWFIRM), UKIRT (WFCAM), Spitzer (IRAC)

#### REFERENCES

- Adelberger, K. L., Steidel, C. C., Shapley, A. E., Hunt, M. P., Erb, D. K., Reddy, N. A., & Pettini, M. 2004, *ApJ*, 607, 226
- Atek, H., Malkan, M., McCarthy, P., et al. 2010, *ApJ*, 723, 104
- Atek, H., Siana, B., Scarlata, C., et al. 2011, *ApJ*, 743, 121
- Barger, A. J., Cowie, L. L., & Wang, W.-H. 2008, *ApJ*, 689, 687
- Basu-Zych, A. R., Hornschemeier, A. E., Hoversten, E. A., Lehmer, B., & Gronwall, C. 2011, *ApJ*, 739, 98
- Bertin, E., & Arnouts, S. 1996, *A&AS*, 117, 393
- Brammer, G. B., van Dokkum, P. G., & Coppi, P. 2008, *ApJ*, 686, 1503
- Bruzual, G., & Charlot, S. 2003, *MNRAS*, 344, 1000
- Calzetti, D., Armus, L., Bohlin, R. C., Kinney, A. L., Koornneef, J., & Storchi-Bergmann, T. 2000, *ApJ*, 533, 682
- Chabrier, G. 2003, *PASP*, 115, 763
- Coil, A. L., Blanton, M. R., Burles, S. M., et al. 2011, *ApJ*, 741, 8
- Daddi, E., Cimatti, A., Renzini, A., Fontana, A., Mignoli, M., Pozzetti, L., Tozzi, P., & Zamorani, G. 2004, *ApJ*, 617, 746
- Davis, M., Faber, S. M., Newman, J., et al. 2003, *Proc. SPIE*, 4834, 161
- Faber, S. M., Phillips, A. C., Kibrick, R. I., et al. 2003, *Proc. SPIE*, 4841, 1657
- Fabricant, D., Fata, R., Roll, J., et al. 2005, *PASP*, 117, 1411
- Fazio, G. G., Hora, J. L., Allen, L. E., et al. 2004, *ApJS*, 154, 10
- Franx, M., Labbé, I., Rudnick, G., et al. 2003, *ApJ*, 587, L79
- Fujita, S. S., Ajiki, M., Shioya, Y., et al. 2003, *ApJ*, 586, L115
- Gawiser, E., Francke, H., Lai, K., et al. 2007, *ApJ*, 671, 278
- Haberzettl, L., Williger, G., Lehnert, M. D., Nesvadba, N., & Davies, L. 2012, *ApJ*, 745, 96
- Jansen, R. A., Franx, M., & Fabricant, D. 2001, *ApJ*, 551, 825
- Hathi, N. P., Ryan, R. E., Jr., Cohen, S. H., et al. 2010, *ApJ*, 720, 1708
- Hicks, E. K., Malkan, M. A., Teplitz, H. I., McCarthy, P. J., Yan, L. 2002, *ApJ*, 581, 205
- Hippelein, H., Maier, C., Meisenheimer, K., et al. 2003, *A&A*, 402, 65
- Hopkins, A. M. 2004, *ApJ*, 615, 209
- Iye, M., Ota, K., Kashikawa, N., et al. 2006, *Nature*, 443, 186
- Iwamuro, F., Moritani, Y., Yabe, K., et al. 2011, *PASJ*, in press (arXiv:1111.6746)
- Kashikawa, N., Aoki, K., Asai, R., et al. 2002, *PASJ*, 54, 819
- Kashikawa, N., Shimasaku, K., Yasuda, N., et al. 2004, *PASJ*, 56, 1011
- Kashikawa, N., Shimasaku, K., Malkan, M. A., et al. 2006, *ApJ*, 648, 7
- Kashikawa, N., Shimasaku, K., Matsuda, Y., et al. 2011, *ApJ*, 734, 119
- Kennicutt, R. C., Jr. 1992, *ApJ*, 388, 310
- Kennicutt, R. C. 1998, *ARA&A*, 36, 189
- Kimura, M., Maihara, T., Iwamuro, F., et al. 2010, *PASJ*, 62, 1135
- Kornei, K. A., Shapley, A. E., Martin, C. L., et al. 2012, *ApJ*, submitted (arXiv:1205.0812)
- Kriek, M., van Dokkum, P. G., Labbé, I., Franx, M., Illingworth, G. D., Marchesini, D., & Quadri, R. F. 2009, *ApJ*, 700, 221
- Lee, J. C., Ly, C., Spitler, L., et al. 2012, *PASP*, in press (arXiv:1205.0017)
- Ly, C., Malkan, M. A., Kashikawa, N., et al. 2007, *ApJ*, 657, 738 [L07]
- Ly, C., Malkan, M. A., Treu, T., et al. 2009, *ApJ*, 697, 1410
- Ly, C., Malkan, M. A., Hayashi, M., et al. 2011, *ApJ*, 735, 91
- Ly, C., Malkan, M. A., Kashikawa, N., et al. 2012, *ApJ*, 747, L16
- Madau, P. 1995, *ApJ*, 441, 18
- Malkan, M. A., Teplitz, H., & McLean, I. S. 1996, *ApJ*, 468, L9
- Miyazaki, S., Komiyama, Y., Sekiguchi, M., et al. 2002, *PASJ*, 54, 833
- Nagao, T., Sasaki, S. S., Maiolino, R., et al. 2008, *ApJ*, 680, 100
- Nakajima, K., Ouchi, M., Shimasaku, K., et al. 2012, *ApJ*, 745, 12
- Oesch, P. A., Bouwens, R. J., Carollo, C. M., et al. 2010, *ApJ*, 725, L150
- Oke, J. B. 1974, *ApJS*, 27, 21
- Ota, K., Iye, M., Kashikawa, N., et al. 2008, *ApJ*, 677, 12
- Ouchi, M., Shimasaku, K., Okamura, S., et al. 2004, *ApJ*, 611, 660
- Pforr, J., Maraston, C., & Tonini, C. 2012, *MNRAS*, in press (arXiv:1203.3548)
- Salpeter, E. E. 1955, *ApJ*, 121, 161
- Shim, H., Colbert, J., Teplitz, H., et al. 2009, *ApJ*, 696, 785
- Sobral, D., Best, P. N., Matsuda, Y., et al. 2012, *MNRAS*, 420, 1926
- Steidel, C. C., & Hamilton, D. 1992, *AJ*, 104, 941
- Straughn, A. N., Kuntschner, H., Kümmel, M., et al. 2011, *AJ*, 141, 14
- Teplitz, H. I., Malkan, M., & McLean, I. S. 1998, *ApJ*, 506, 519
- Xia, L., Malhotra, S., Rhoads, J., et al. 2011, *AJ*, 141, 64
- Yagi, M., Kashikawa, N., Sekiguchi, M., Doi, M., Yasuda, N., Shimasaku, K., & Okamura, S. 2002, *AJ*, 123, 66